On the detectability of internal waves by an imaging lidar

J. M. Magalhaes,[1,2] J. C. B. da Silva,[1,2] M. Batista,[2] L. Gostiaux,[3] T. Gerkema,[4] A. L. New,[5] and D. R. G. Jeans[6]

[1] The first results of a multisensor airborne survey conducted off the western Iberian Coast are presented (including visible, lidar, and infrared imagery) and reveal the presence of internal solitary waves (ISWs) propagating into the nearshore region. For the first time, two-dimensional lidar imagery is shown to detect the presence of ISWs, and the results are interpreted in a more comprehensive framework provided by the remaining instrumentation. Sea surface roughness patterns, resulting from the ISWs, are found to be imaged in the lidar data, where specular reflection causes slicks to appear as areas of significantly reduced backscatter. Moreover, the lidar data reveal an unprecedented view into the ISW surface and subsurface structures. Possible interpretations are discussed based on the accumulation of surfactants and air bubble entrainment at the leading edge of the ISWs (where maximum convergence occurs). Citation: Magalhaes, J. M., J. C. B. da Silva, M. Batista, L. Gostiaux, T. Gerkema, A. L. New, and D. R. G. Jeans (2013), On the detectability of internal waves by an imaging lidar, *Geophys. Res. Lett.*, *40*, 3429–3434, doi:10.1002/grl.50669.

1. Introduction

[2] Remote sensing has been revealing that internal solitary waves (ISWs) are not isolated events, but rather ubiquitous features in the world's oceans [e.g., *Jackson et al.*, 2012]. In particular, satellite observations (especially from synthetic aperture radar, SAR) have been providing important insights into a unified understanding of the ISWs generation, propagation, and dissipation mechanisms [e.g., *da Silva et al.*, 2011]. In this case, the ISWs imaging mechanism relies on sea surface roughness manifestations, resulting essentially from the near-surface velocity perturbations induced by the ISW velocity field [*Alpers*, 1985].

[3] However, satellite imagery is usually unable to reveal the full structure of the ISWs dissipation and breaking processes (typically occurring as ISWs propagate over the

shelf and into shallower waters) [e.g., *Moum et al.*, 2003; *Shroyer et al.*, 2010], owing mainly to the small space scales which are found during these stages. Overcoming these limitations would provide us with a deeper understanding of the ultimate fate of the energy contained in ISWs. For that matter, airborne remote sensing has been proving to be a suitable alternative to satellite measurements, where increased spatial resolutions can be used to survey a given area almost continuously in time. For instance, ISW sea surface temperature (SST) patterns inferred from airborne thermal infrared (IR) imagery have already been widely explored in the literature, and these have confirmed the intricate turbulent character of breaking ISWs [e.g., *Farrar et al.*, 2007; *Marmorino et al.*, 2004, 2008].

[4] Airborne surveying of ISWs has also been done using lidar (light detection and ranging) measurements, which have also been able to detect their presence [*Churnside and Ostrovsky*, 2005; *Churnside et al.*, 2012]. However, these studies used single beam (nadir viewing) instruments, working with green light (532 nm) that can only provide a one-dimensional (1-D) view of the ISWs subsurface structure—since ISWs are seen via oscillations in thin layers of phytoplankton. In other words, the 2-D horizontal structure of ISWs has not yet been explored with 2-D lidar instruments, which until now have only been used for ocean and coastal monitoring surveys [*Reineman et al.*, 2009].

[5] Therefore, this paper presents the first results of an airborne campaign (A.NEW – Airborne observations of the Nonlinear Evolution of internal Waves generated by internal tidal beams) undertaken in the Estremadura Promontory (off the western Iberian Coast, see Figure 1), where high ISW activity has already been reported [*Magalhaes and da Silva*, 2012]. Evidence of ISW sea surface signatures in 2-D lidar measurements is presented (together with visible and thermal IR data), and new insights into the surface and subsurface structure of the ISWs are discussed.

2. Methodology and Instrumentation

[6] A comprehensive satellite data set acquired over the western Iberian Coast was used to plan a detailed ISW synergetic survey using satellite (SAR imagery) and airborne measurements. A composite map resulting from this data set is shown in Figure 1a, where ISW wavefronts in the nearshore region are seen propagating almost in a west-east direction, along gently varying bathymetry and into increasingly shallow waters [see, *Magalhaes and da Silva*, 2012].

[7] Figure 1b shows a TerraSAR-X image (acquired 14 July 2010, nearly coincident in time with our measurements) with a typical view of the incoming ISW field propagating toward shore. Also shown is the flight track of the twin propeller Dornier 228 from the Natural Environment Research Centre, used in a 2 day surveying campaign during

[1]Interdisciplinary Centre of Marine and Environmental Research, CIMAR, Porto, Portugal.
[2]Department of Geosciences, Environment and Spatial Planning, University of Porto, Porto, Portugal.
[3]Laboratoire de Mécanique des Fluides et d'Acoustique, UMR5509, CNRS/Université de Lyon, Lyon, France.
[4]Royal Netherlands Institute of Sea Research, Texel, Netherlands.
[5]Marine Systems Modelling Group, National Oceanography Centre, Southampton, UK.
[6]Oceanalysis, Wallingford, UK.

Corresponding author: J. C. B. da Silva, Department of Geosciences, Environment and Spatial Planning, University of Porto, Porto 4169-007, Portugal. (jdasilva@fc.up.pt)
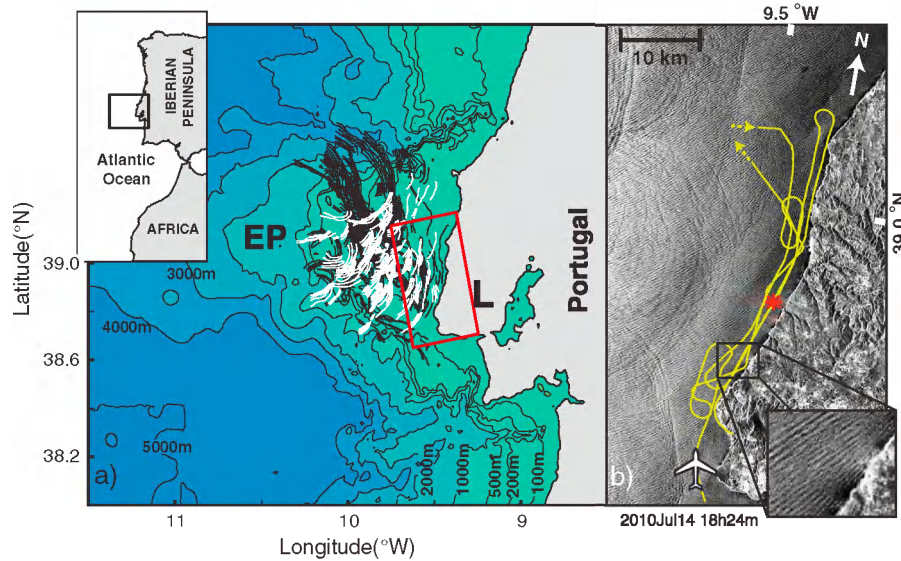
Figure 1. (a) Bathymetry of the Estremadura Promontory region (see EP and black square in the upper-left inset) together with a composite map of the ISW field (where solid white and black lines represent ISW wavefronts coming from the northern and southern flanks of EP, respectively). L points to the location of Lisbon. (b) TerraSAR-X image acquired on 14 July 2010 at 18 h, 24 min UTC (red rectangle in Figure 1a). The yellow strip represents the aircraft's track on 16 July 2010, and an enlarged view of the black rectangle (with approximately $4 \times 5\,\text{km}^2$) is shown on the lower right corner of Figure 1b. The red star points to the location of Figure 2a.

the summer of 2010 (15 and 16 July—only the flight track for 16 July is shown). Multiple flight passes were made (nominal flight altitude of 500 m) that essentially covered a nearshore strip (200–3 km offshore) with an extent of approximately 40 km in the alongshore direction. Sea surface patterns indicating the presence of ISWs were tracked by the onboard crew (see Figure 2a), who were assisted on the first day by near real-time satellite acquisitions (relayed to the aircraft via radio communications). Airborne high-resolution imaging sensors were then used to observe the nearshore evolution of the ISWs as they propagated toward shore. The instrumentation included the following:

[8] 1. A high-resolution digital camera (RCD105) with 39×10^6 pixels (yielding a pixel spacing less than 10 cm), with a high sampling rate allowing overlapping in successive images, and a swath width of approximately 410 m.

[9] 2. A thermal IR camera (TABI-320) operating in the spectral range 8–12 μm, with a thermal resolution of 0.02° C, a nominal ground resolution of 1.5 m, and a swath width of approximately 480 m.

[10] 3. A lidar scanning system (Leica ALS50-II, operating at 1064 nm—i.e., near IR) with a pulse rate greater than 20 kHz, which provides a 2-D view of the sea surface elevation, with horizontal and vertical resolutions of approximately 1 and 0.15 m, respectively, and a swath width of approximately 270 m.

[11] All the instrumentation was integrated with the lidar GPS navigation system, and therefore geographic referencing was made on the same basis for all the images.

[12] Flight dates were set for spring tides (when ISWs are more frequently observed) and flight times chosen on a daily basis in order to maximize cloud-free observations (e.g., 13–16 h for 16 July—local time). During the flight, the surface air temperatures were around 25°C, and low to moderate winds (below 4 m/s) were blowing from the NW. No

significant precipitation occurred during the day of the flight or in the previous days, and the wavelength of local swell waves incident from the NW was set at approximately $200 \pm 50\,\text{m}$ (see Figure 1b, inset).

3. Results

[13] Figure 2 presents an overview of part of the airborne survey made on 16 July (i.e., focusing on the area near the center of the black square in Figure 1b). Figure 2a shows an example of an ISW packet propagating toward shore at the time of the measurements (see red star in Figure 1b for location), while Figure 2b presents a view of the incoming waves as they approach the very nearshore regions (as seen by the airborne high-resolution visible imagery), propagating in shallow waters just 1 km offshore.

[14] A close inspection of Figure 2b reveals several elongated sea surface signatures (marked with arrows and labeled S_1, S_2, and S_3), where lighter and darker areas correspond to the alternating sea surface roughness patterns of the incoming ISWs (propagating from left to right, toward shore). These dominant features have separation distances of $O(100)$ m and extend in the alongshore direction for almost 1 km (from SW to NE, although they extend further beyond the visible mosaic). It is also noteworthy that the darker bands (with decreased brightness, typical of slick-like surfaces) become increasingly harder to discriminate as these features move toward shore (owing to sunglint in the left part of the visible mosaic). At the same time, the most shoreward segments also have the presence of white "foamy" lines (seen best in S_2 and S_3, but also in the northern end of S_1), which seem to concentrate essentially in the leading edge of the darker slick-like bands (seen best in S_2).

[15] A simultaneous SST view is shown in Figure 2c, where the area corresponding to the visible mosaic is shown
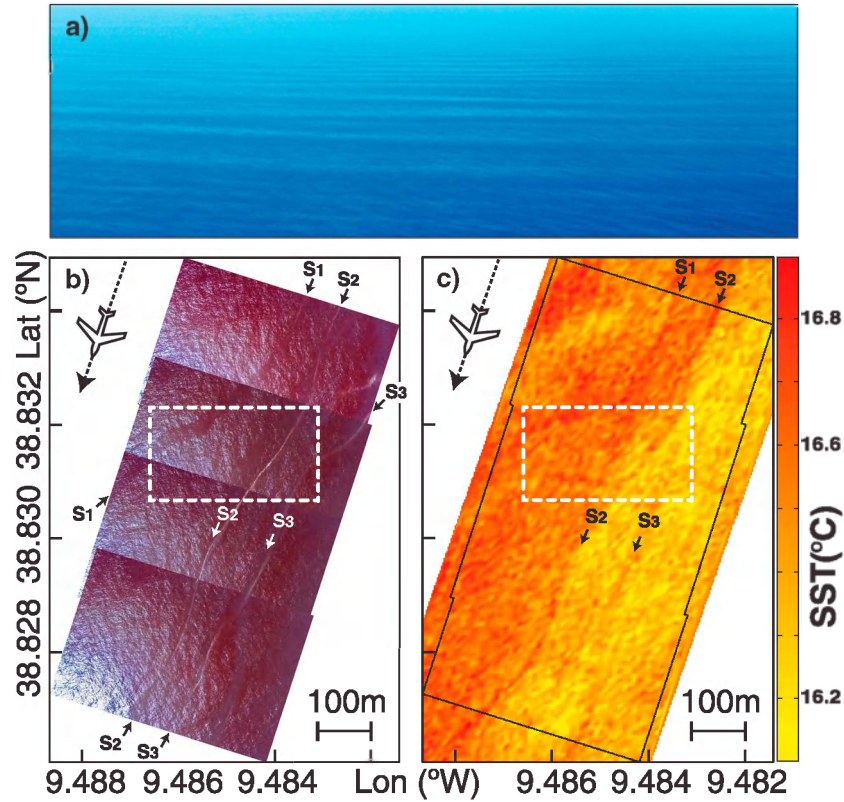
Figure 2. (a) Photograph of an ISW packet travelling toward shore (see red star in Figure 1b). (b) Visible (high-resolution) photographic mosaic showing ISW surface signatures tracked nearshore (acquired at the center of the black square in Figure 1b and labeled S_1 to S_3). (c) IR SST strip, where the region surveyed in Figure 2b is shown as a black solid frame. The locations of S_1, S_2, and S_3 are also shown. The flight path direction is indicated on the top left corner of Figures 2b and 2c.
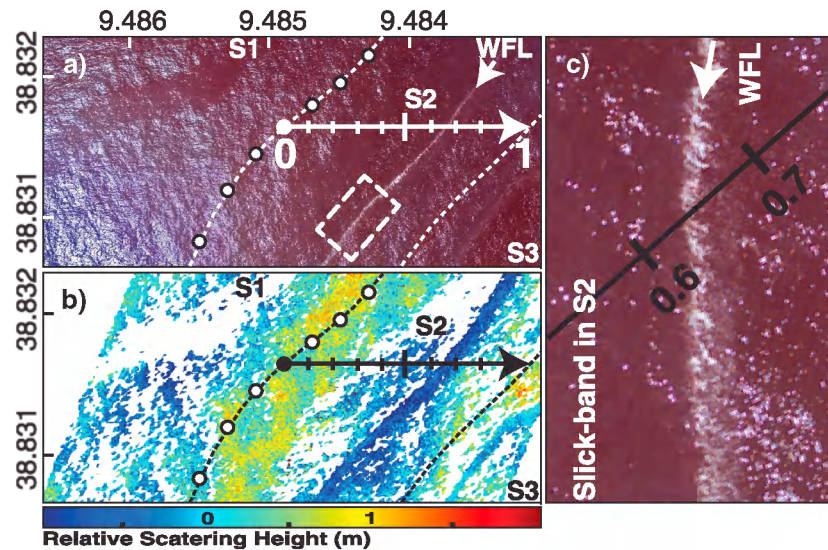

Figure 3. Detailed view of ISWs in the very nearshore area (≈ 1 km offshore), corresponding to the area in the dashed rectangles in Figure 2. (a) High-resolution visible imagery. (b) Lidar relative scattering height data (with respect to the mean value of the image). (c) A zoom made in the area depicted by the white dashed rectangle in Figure 3a. The position of the white foam line (WFL) is marked with an arrow and labeled WFL. For reference, a transect is shown with its normalized coordinates using an arrow in Figures 3a and 3b, and all profiles shown in Figure 4 are marked using white circles to define their point of origin and assumed to extend between the dashed lines.
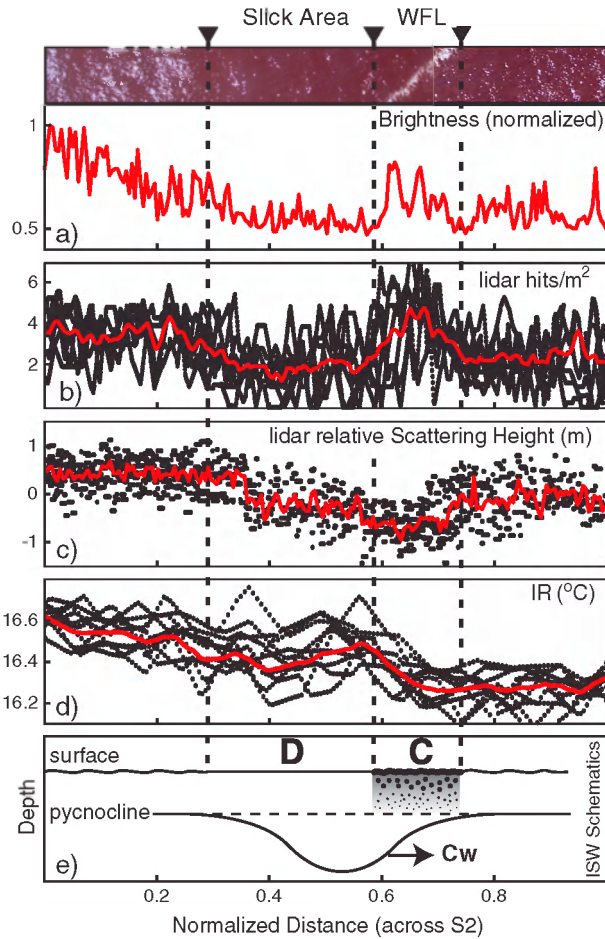
Figure 4. Profiles for transects (seven in total) made across S_2 (between the dashed lines in Figure 3) as a function of normalized coordinates (i.e., 0 and 1 mark left and right boundaries, respectively). (a) High-resolution strip from Figure 3a together with the mean brightness for all profiles. (b) Returned hits per unit area in the lidar backscattered data. (c) Lidar RSH data. (d) IR SST data. (e) Schematic view of an ISW according to our interpretation of the multisensor data (C_w marks the direction of propagation, and the areas of velocity divergence and convergence are labeled D and C). In Figures 4b–4d, red lines represent averages for all profiles made across S_2.

by a solid black frame, and the locations of S_1, S_2, and S_3 are also indicated. This joint view of thermal IR and visible imagery reveals that the elongated features appear as narrow lines with localized warmer SST signatures (roughly 0.5°C warmer than the undisturbed colder medium ahead of S_3). We note in passing that these results are consistent with those obtained in Juan the Fuca Strait [*Marmorino et al.*, 2008]) for breaking ISWs and further support our interpretation of the visible imagery.

[16] A detailed view of these features is shown in Figure 3a, where the area depicted by the dashed rectangles in Figure 2 was enlarged to provide a clearer view of the slick-like bands (in S_1 and S_2) and the white foam lines stretching along them (in S_2). At the same time, the corresponding lidar image depicting the relative scattering heights (RSHs hereafter) is also shown in Figure 3b, and it reveals that the slicks in S_1 and S_2 are associated with regions

of reduced backscatter (white areas representing low backscatter signal ≤ 1 hits/m^2), while the well-formed foam line in S_2 is marked with a line of decreased RSH (i.e., Figure 3b, dark blue line). A detailed view of the area surrounding the foam line is shown in Figure 3c (see Figure 3a, white rectangle), revealing its white "foamy" character generally ahead of the slick-like band seen in S_2.

[17] To further inspect these results, several transects were made across S_2 (with a time difference less than 10 s), between the dashed curves where one slick band and one foam line are included, and analyzed using the multisensor data acquired during the flight (i.e., visible imagery, lidar, and thermal IR). To make a consistent analysis, a total of seven west-east transects were taken individually, which essentially covered the north-south extent of S_2 (such as the one in Figure 3 marked by the horizontal arrows). This means that each transect extends from left to right (across the slick and the white "foamy" line), while different transects span the area of interest from top to bottom.

[18] These results are presented in Figure 4 in normalized coordinates—i.e., considering the left and right boundaries are taken from the dashed curves in Figure 3, and these are always set to 0 and 1, respectively (according to the vertical ticks in the arrows). Figure 4a presents an image strip taken from Figure 3a (matching the transect location marked by the white arrow), together with an average for all profiles made in the visible imagery (red curve). A slight decrease in brightness can be seen approximately between 0.3 and 0.6, which characterizes our interpretation of the slick area, whereas a clear and sharp increase in brightness matches with the location of the white "foamy" line (note that sunglint causes a general west-east decrease in brightness). At the same time, the lidar data show that the slick is seen as a decrease in the amount of backscattered signal (seen in Figure 4b via the number of returned hits/m^2), while it is also associated with a slight decrease in the RSH (Figure 4c), in comparison with the area behind the slick. On the other hand, the RSH values reach their minimum at the location of the foam line, where the number of hits increases locally between 0.6 and 0.75. In Figure 4d (where profiles were taken from Figure 2c, in a manner consistent with those already discussed), the thermal IR data reveal a transition area matching with the location of the foam line, which lies between a colder area in front (ahead of the propagating features) and a warmer area behind. Finally, our interpretation of an ISW propagating along the pycnocline and inferred from our airborne surface data is presented in Figure 4e. Note the surface divergence (D) and convergence (C) areas matching the slick and foam line areas, respectively; the areas of divergence and convergence are those expected from a simple consideration of the velocity structure in a propagating mode-1 ISW of depression, as those typically observed in this region [see, e.g., *Quaresma et al.*, 2007].

4. Discussion and Conclusions

[19] An airborne multisensor image survey off the west coast of Lisbon (Portugal, where high ISW activity has already been reported) [*Magalhaes and da Silva*, 2012] revealed the presence of ISW sea surface signatures propagating into the very nearshore region (considered here as under 1 km offshore). Simultaneous high-resolution visible imagery and IR SST data (Figure 2) revealed similar

surface signatures to those obtained for other ISWs in their final propagation stages. According to the mechanisms described in *Marmorino et al.* [2008], these consist of dipolar thermal structures with narrow warm fronts ahead of trailing colder wakes. However, we note in passing that, while similar structures to those presented by *Marmorino et al.* [2008] were also found farther offshore (see event A in their Figure 4 with a larger ISW), our results are more like their events B and C (with smaller-scale ISWs), which are much closer to shore and in shallower waters.

[20] The main novelty present here consists in including 2-D lidar surface image data to the multisensor suite usually used to measure ISWs in the near-coastal zone. On the one hand, Figures 3 and 4 clearly illustrate the ability of the lidar to reveal the presence of surface slicks, which in turn indicate the presence of ISW sea surface roughness patterns. In fact, the imaging mechanism which enables ISWs to be detected in the lidar is somewhat similar to the one in SAR, since surface slicks are made visible via the lack of backscattered signal—lost to specular reflection typical in slick areas. On the other hand, the lidar in the near-IR range benefits from its limited ability to penetrate into the seawater (maximum penetration depth is on the order of a few centimeters), which makes it ideal to observe surface and very shallow subsurface structures—such as those induced by the ISWs turbulent character. Indeed, Figures 3 and 4 show that the white foam lines are also imaged in the lidar data as narrow lines of reduced RSH, which are found (on average) 1 m "below" the surrounding areas—seen consistently throughout the data set, regardless of the long waves (i.e., swell), which could potentially mask some of these results. However, these sudden decreases in the scattering height need to be carefully interpreted, since they cannot result directly from sea surface depressions, nor can they be related with some artifact owing to the presence of swell waves.

[21] We now briefly discuss the effects of surfactants and air bubble entrainment at the leading edge of the ISWs, where strong convergence and vertical downwelling take place, as a possible explanation for these lines of decreased RSH. Recent measurements and numerical modeling [*Serebryany and Galybin*, 2009; *Grimshaw et al.*, 2010] have already accounted for the presence of air bubbles that are entrained over the leading slopes of the ISWs. Furthermore, strong entrainment of air bubbles (several tens of meters deep) has also been measured in downwelling currents generated at tidal fronts [*Baschek and Farmer*, 2010]. Based on previous work [see e.g., *Churnside*, 2010], which shows that the presence of bubbles coated with surfactants increases the backscatter to a considerable extent, we expect the foam and bubbles concentrated near the maximum convergence zone associated with the internal wave at the surface to be capable of increasing the lidar backscatter. This would explain the lidar signal coherence observed along the foam lines.

[22] We also note in passing that *Marmorino et al.* [2004] measured similar foam lines at the leading edge of ISWs, with colder SST signatures (presumably owing to increasing evaporation) that are consistent with the temperature profile of the foam line seen in our Figure 4d.

[23] We next make some comments on possible explanations for the RSH decreased values over the foam lines. These may be related with the optical properties of seawater in the presence of air bubbles and surfactants. The decreased

values of RSH may be interpreted as an increase in the "path length" of the lidar signal (measured at the white foam lines, i.e., apparently "deeper" RSH signatures), which could result from multiple reflections occurring inside the surfactant foam features—in analogy with the well-known "hail spike" phenomenon in weather radars [see e.g., *Wilson and Reum*, 1988], which is a result of multiple scattering in convective cells and at the ground. Since the surfactant foam lines are thin features, we propose that the IR radiation can be transmitted and reflected within the foam surface layer before reemerging into the lidar direction. Although the role of surfactants (aggregated at the foam line) in the optical path length is poorly understood in the configuration of our lidar, we suggest that these could contribute to a surfactant bubble coating, known to increase significantly the backscattered lidar signals [see above, and in *Churnside*, 2010].

[24] On the other hand, *Krekova et al.* [2004] modeled the power of the lidar backscattering signal under the influence of subsurface air bubbles. Although their results were based on green light ($\lambda = 0.53\ \mu m$), they concluded that the backscattered signal from the subsurface layers could increase by an order of magnitude owing to the presence of air bubbles, whose influence on the lidar return was traced to depths (up to 15 m) significantly greater than the original penetration depth (with a total extinction coefficient of $0.22\ m^{-1}$, see their Figure 2). Unfortunately, there are no studies concerning the water penetration depths of near-IR lidar radiation in the presence of air bubbles, and we will not discuss this mechanism further here. Finally, it is also possible that some combination of the two mechanisms referred above could be at work.

[25] In summary, the multisensor data painted a consistent picture, where sea surface signatures of ISWs were observed to propagate into the very nearshore areas. While the lidar imaging mechanism for ISWs is qualitatively similar to other active radar-based imaging sensors, the RSH lidar images appear to reveal part of the 3-D shallow subsurface structure, thus promising additional insights into the final dissipation (or even breaking) stages of the ISWs. In particular, 2-D lidar data seem to reveal evidence of surfactants and enhanced air bubble entrainment in the leading edge of the ISWs, where the areas of maximum convergence and vertical downwelling are concentrated. This would mean that lidar data may be used to study further into the small-scale processes involving air-sea interactions. In particular, a deeper penetrating lidar could be used to evaluate the extent of (possibly surfactant coated) bubble entrainment at the leading edge of ISWs. Further studies are needed to confirm or challenge the hypotheses proposed here to explain the lidar imaging mechanism of the foam lines.

References

Alpers, W. (1985), Theory of radar imaging of internal waves, *Nature*, *314*, 245–247, doi:10.1038/413245a0.

Baschek, B., and D. M. Farmer (2010), Gas bubbles as oceanographic tracers, *J. Atmos. Oceanic Technol.*, *27*, 241–245, doi:10.1175/2009JTECHO688.1.

Churnside, J. H. (2010), Lidar signature from bubbles in the sea, *Opt. Express*, *18*(8), 8294–8299, doi:10.1364/OE.18.008294.

Churnside, J. H., and L. A. Ostrovsky (2005), Lidar observation of a strongly nonlinear internal wave train in the Gulf of Alaska, *Int. J. Remote Sens.*, *26*(1), 167–177, doi:10.1080/01431160410001735076.

Churnside, J. H., R. D. Marchbanks, J. H. Lee, J. A. Shaw, A. Weidemann, and P. L. Donaghay (2012), Airborne lidar detection and characterization of internal waves in a shallow Fjord, *J. Appl. Remote Sens.*, *6*, 063611, doi:10.1117/1.JRS.6.063611.

da Silva, J. C. B., A. L. New, and J. M. Magalhaes (2011), On the structure and propagation of internal solitary waves generated at the Mascarene Plateau in the Indian Ocean, *Deep Sea Res., Part I*, *58*, 229–240, doi:10.1016/j.dsr.2010.12.003.

Farrar, J. T., C. J. Zappa, R. A. Weller, and A. T. Jessup (2007), Sea surface temperature signatures of oceanic internal waves in low winds, *J. Geophys. Res.*, *112*, C06014, doi:10.1029/2006JC003947.

Grimshaw, R. H. J., K. R. Khusnutdinova, L. A. Ostrovsky, and A. S. Topolnikov (2010), Structure formation in the oceanic subsurface bubble layer by an internal wave field, *Phys. Fluids*, *22*, 106603, doi:10.1063/1.3499379.

Jackson, C. R., J. C. B. da Silva, and G. Jeans (2012), The generation of nonlinear internal waves, *Oceanography*, *25*(2), 108–123, doi:10.5670/oceanog.2012.46.

Krekova, M. M., G. M. Krekov, and V. S. Shamanaev (2004), Influence of air bubbles in seawater on the formation of lidar returns, *J. Atmos. Oceanic Technol.*, *21*, 819–824, doi:10.1175/1520-0426(2004)021<0819:IOABIS>2.0.CO;2.

Magalhaes, J. M., and J. C. B. da Silva (2012), SAR observations of internal solitary waves generated at the Estremadura Promontory off the west Iberian coast, *Deep Sea Res., Part I*, *69*, 12–24, doi:10.1016/j.dsr.2012.06.002.

Marmorino, G. O., G. B. Smith, and G. J. Lindemann (2004), Infrared imagery of ocean internal waves, *Geophys. Res. Lett.*, *31*, L11309, doi:10.1029/2004GL020152.

Marmorino, G. O., G. B. Smith, J. H. Bowles, and W. J. Rhea (2008), Infrared imagery of 'breaking' internal waves, *Cont. Shelf Res.*, *28*, 485–490, doi:10.1016/j.csr.2007.10.007.

Moum, J. N., D. M. Farmer, W. D. Smyth, L. Armi, and S. Vagle (2003), Structure and generation of turbulence at interfaces strained by internal solitary waves propagating shoreward over the continental shelf, *J. Phys. Oceanogr.*, *33*, 2092–2112, doi:10.1175/1520-0485(2003)033<2093:SAGOTA>2.0.CO;2.

Quaresma, L. S., J. Vitorino, A. Oliveira, and J. da Silva (2007), Evidence of sediment resuspension by nonlinear internal waves on the western Portuguese mid-shelf, *Mar. Geol.*, *246*, 123–143, doi:10.1016/j.margeo.2007.04.019.

Reineman, B. D., L. Lenain, D. Castel, and W. K. Melville (2009), A portable airborne scanning lidar system for ocean and coastal applications, *J. Atmos. Oceanic Technol.*, *26*, 2626–2641, doi:10.1175/2009JTECHO703.1.

Serebryany, A., and N. Galybin (2009), Observations of the effect of internal waves on subsurface layer of air bubbles in the sea, in *Proceedings of the Third International Conference on Underwater Acoustic Measurements: Technologies and Results*, Nafplion, Greece, 22–26 June 2009, edited by J. Papadakis, and L. Bjorno. (Available at http://promitheas.iacm.forth.gr/UAM_Proceedings/uam2009/17-10.pdf).

Shroyer, E. L., J. N. Moum, and J. D. Nash (2010), Vertical heat flux and lateral mass transport in nonlinear internal waves, *Gephys. Res. Lett.*, *37*, L08601, doi:10.1029/2010GL042715.

Wilson, J. W., and D. Reum (1988), The flare echo: Reflectivity and velocity signature, *J. Atmos. Oceanic Technol.*, *5*, 197–205, doi:10.1175/1520-0426(1988)005<0197:TFERAV>2.0.CO;2.